

# Horizontal structure function and vertical correlation analysis of mesoscale water vapor variability observed by airborne lidar

L. Fischer,<sup>1</sup> G. C. Craig,<sup>1</sup> and C. Kiemle<sup>2</sup>

Received 22 January 2013; revised 29 May 2013; accepted 19 June 2013.

[1] Analysis is presented of airborne lidar measurements of water vapor, covering a height range from 1.5 to 10.4 km, from three field campaigns (midlatitude summer, polar winter, and subtropical summer). The lidar instrument provides two-dimensional cross sections of absolute humidity, with high accuracy (errors less than 5–7%) and high vertical ( $\sim 200$  m) and horizontal ( $\sim 2$  km) resolution. Structure functions, i.e., statistical moments up to the fifth-order of absolute increments over a range of scales, are investigated, and power law scaling or statistical-scale invariance was found over horizontal distances from 5 to 100 km. The scaling exponents are found to take different values, depending on whether or not the observations were taken in an air mass where convective clouds were present. The exponent of the first-order structure function in nonconvective regions,  $H = 0.63 \pm 0.10$ , is large indicating a smooth series with long-range correlations, in contrast to the lower value  $H = 0.35 \pm 0.11$  found in convective air masses. Correspondingly, the moisture field in the convective regime was found to be more intermittent than for the nonconvective regime, i.e., water vapor structures in convectively influenced air mass show more jump discontinuities, which could be explained by the moistening and drying effects of updrafts and downdrafts in convective air mass. Within each regime (convective or nonconvective), the values appear to be universal, with no significant dependence on the season, latitude, or height where the observations were made. Furthermore, some evidence is found that vertical correlation lengths are longer in convective air masses.

**Citation:** Fischer, L., G. C. Craig, and C. Kiemle (2013), Horizontal structure function and vertical correlation analysis of mesoscale water vapor variability observed by airborne lidar, *J. Geophys. Res. Atmos.*, 118, doi:10.1002/jgrd.50588.

## 1. Introduction

[2] Water vapor variability on scales comparable to the finest resolution of climate and weather models is not yet well characterized and understood, despite its great influence on the development of cloud and precipitation processes [Sherwood *et al.*, 2010; Wang *et al.*, 2010]. The lack of understanding of the small-scale dynamics of water vapor throughout the troposphere leads to strong limitations in predicting localized phenomena in weather models. It is known, for example, that forecasting the initiation of deep convection in a cloud-resolving model is highly dependent on high-quality water vapor observations [e.g., Kottmeier *et al.*, 2008]. Furthermore, Tompkins and Berner [2008] and

Zhang *et al.* [2003] have shown that the lack of knowledge of water vapor fluctuations on scales smaller than the model grid leads to errors in the development of deep convection. An important prerequisite for improving the representation of moist processes in weather and climate models is an accurate characterization of tropospheric small-scale water vapor variability, including subgrid-scale humidity fluctuations.

[3] A well-established method for describing the variability of atmospheric parameters is scaling analysis, i.e., scaling behavior is identified in time series as a power law dependence with length scale of structure functions. Numerous studies have presented scaling analyses of atmospheric wind, energy, and temperature, notably a recent study by Waite and Snyder [2012] which has shown that the dynamics of moist processes have a strong impact on the slope of mesoscale kinetic energy spectra. This provides a motivation to investigate water vapor spectra directly. Naively, one might expect water vapor to be transported as a passive scalar, which would lead to a 5/3 slope in the variance spectrum in three-dimensional turbulence [Corrsin, 1951]. However, an increasing number of observational studies shows deviations from this expectation whereby the mechanisms remain controversial [Lovejoy *et al.*, 2010; Kahn *et al.*, 2011; Fischer *et al.*, 2012; Pressel and Collins, 2012].

<sup>1</sup>Institute of Meteorology, Ludwig-Maximilians University, Munich, Germany.

<sup>2</sup>Institute of Atmospheric Physics, Deutsches Zentrum für Luft- und Raumfahrt Wessling, Oberpfaffenhofen, Germany.

Corresponding author: L. Fischer, Institute of Meteorology, Ludwig-Maximilians University, Theresienstraße 37, Munich 80333, Germany. (lucas.fischer@lmu.de)

[4] Structure functions and power spectra are often used as powerful tools to characterize scale-dependent variability of an atmospheric field (e.g., horizontal wind, kinetic energy, potential temperature, and water vapor), as mentioned above. In particular, if the structure function or power spectrum of an atmospheric field has power law dependence over a range of spatial scales, then scaling is an indicator of statistical scale invariance, e.g., an atmospheric field can be described by a certain cascade. While the power spectrum method only describes variance spectra (i.e., second-order functions) for stationary time series, structure functions can be used to explore scaling laws of higher orders, in nonstationary, intermittent situations [e.g., *Pierrehumbert*, 1996; *Cho et al.*, 2000; *Lovejoy et al.*, 2010; *Fischer et al.*, 2012].

[5] To date, there are only few studies analyzing the spatial-scale dependence of tropospheric water vapor fluctuations in terms of scaling exponents. In the following, we apply the Wiener-Khinchin Theorem to transform the spectral slope values into second-order structure function scaling exponents by subtracting the value one [*Monin and Yaglom*, 1975]. In the late 1980s, *Nastrom et al.* [1986] computed power spectra of water vapor mixing ratio airborne in situ measurements at heights from 9 to 14 km. They found a range of values from two thirds (the predicted value for a passive tracer in three-dimensional turbulence) up to one from 150 to 1500 km in horizontal range. In the 1990s, *Tjemkes and Visser* [1994] analyzed satellite measurements of specific humidity and found exponents similar to those of *Nastrom and Gage*. *Cho et al.* [1999, 2000] enlarged the set of mesoscale scaling exponents (6–60 km and 0.05–100 km) in two aircraft studies with in situ measurements, suggesting that the values of the exponents differ between the boundary layer, the tropical free troposphere, and the extratropical free troposphere. In summary, they found values from two thirds up to values larger than one with different intermittency in different regions, e.g., higher values in the tropics. In the last 3 years, several studies have been published where satellite data for water vapor from the Atmospheric Infrared Sounder were analyzed [*Kahn et al.*, 2009, 2011; *Pressel and Collins*, 2012]. In particular, *Pressel and Collins* [2012] show the presence of two distinct scaling regimes, one which characterizes the spatial variability of water vapor in the boundary layer and one in the free troposphere. Boundary layer exponents in the horizontal range from 50 to 500 km are found to be near two thirds, while free tropospheric scaling exponents are found to be generally greater than one. In the same year, *Fischer et al.* [2012] examined airborne lidar water vapor time series classified according to whether or not convective clouds occurred in the observed air mass. They found a separation of the scaling exponents with values close to two thirds in the convective air masses and values around one in other air masses (usually at upper levels).

[6] The flatter spectral slope observed in boundary layer and convective air masses could be a consequence of vertical injection of moisture anomalies on small scales by convective eddies, leading to greater variability on small scale than is found in air masses that are dominated by large-scale advective processes. However, much uncertainty remains in the details of such a mechanism, particularly concerning a quantitative theory for the scaling exponents. Nevertheless, a height-resolved scaling law statistic can be of practical use for improving stochastic parameterizations

that attempt to explicitly describe subgrid variability [e.g., *Calif*, 2011], for example, the development of cascade-based stochastic downscaling methodologies [*Harris et al.*, 2001]. *Cusack et al.* [1999] showed that the use of scaling laws to extrapolate variability to unresolved scales can reduce model biases concerning water vapor, temperature, and cloud amount in the troposphere.

[7] The previous studies of water vapor variability discussed above have important limitations. Airborne in situ measurements provide a single time series at nearly constant height, which can only be compared to data from other heights taken at different locations or times. In contrast, two-dimensional airborne lidar observations can be analyzed throughout the troposphere, i.e., a height-resolved analysis of scaling exponents with a vertical resolution of 150–200 m is possible. But data coverage is limited to particular measurement campaigns where the instrument was deployed. Satellite observations provide global coverage and are height-resolved, but the horizontal ( $\sim 50$  km) and vertical resolution ( $\sim 3$  km) is much coarser than for airborne lidar measurements and also coarser than the grid scale of most weather and climate models for which one would like to have data. A full understanding of water vapor variability in the troposphere will draw on the complementary strengths of the various data sources.

[8] The paper focuses on the particular strengths of airborne lidar data, namely high horizontal and vertical resolution, to characterize the scaling behavior of water vapor in different air masses. The work extends the preliminary results of *Fischer et al.* [2012] who identified different scaling laws for convective and nonconvective air masses sampled during a field campaign over western Europe in summertime. Here the analysis is extended to include data from subtropical and polar regions in autumn and winter, respectively. This increases the total amount of data by a factor of 5, but more importantly, samples different atmospheric regimes. The conclusion of *Fischer et al.* [2012] that the scaling exponents of water vapor structure functions showed two regimes, often separated by a sharp boundary in height, will be reassessed in this larger data set. The primary scientific objective will be to determine whether these two regimes are universal, or if additional behaviors are found in other meteorological situations. In addition, a preliminary analysis of vertical correlations for two flight segments will be presented, to test the hypothesis that vertically coherent injections of moisture in convective air masses will lead to stronger vertical correlations than those found in nonconvective air masses where advection shears out vertical structures.

[9] After giving an overview on the airborne lidar data set in section 2, the structure function method will be discussed in section 3. The results of three campaigns in different regions of the world and times of the year are subsequently shown in section 4. Section 5 presents a height-correlation analysis of airborne lidar observations. In section 6, the results of the campaigns are discussed and conclusions are stated.

## 2. The Airborne Lidar Data Set

[10] The airborne differential absorption lidar (DIAL) instrument for water vapor observations was developed at

**Table 1.** Overview of the Three Campaigns COPS/ETReC, T-PARC, and IPY-THORPEX

	COPS/ETReC	T-PARC	IPY-THORPEX	Total
Latitude/longitude	41°N–49°N/7.5°W–10°E	24°N–40°N/129°E–152°E	53°N–81°N/2°E–25°E	
Date	8 Jul 2007 to 1 Aug 2007	1 Sept 2008 to 1 Oct 2008	25 Feb 2008 to 17 Mar 2008	
Number of flights	7	6	7	20
Segments	97	265	160	522
Height range (km)	2.0–9.8	2.0–10.4	1.5–9.3	
Segment length (km)	225–700	350–1300	330–800	
Total length of time series (km)	44,560	190,560	134,010	369,130

the Deutsches Zentrum für Luft- und Raumfahrt (DLR). The DIAL technique makes use of laser probing of the atmosphere at two wavelengths, including an online wavelength which is placed at an absorption line of water vapor and an off-line wavelength positioned outside of the absorption line to serve as a reference. Specific humidity can be derived from the difference of the backscatter signal received at the two wavelengths using the DIAL equation [Schotland, 1974]. The DIAL technique is described in detail by, e.g., *Werner and Herrmann* [1981] and *Bösenberg* [1998]. In 2007, the newly developed “WALES” four-wavelength water vapor DIAL [Wirth *et al.*, 2009] was deployed for the first time. The WALES (Water Vapour Lidar Experiment in Space) system with three online (two additional) and one off-line wavelengths was built as an airborne demonstrator for a future spaceborne system and has the potential to cover the large humidity variations encountered throughout the troposphere.

[11] In this paper, we analyze the water vapor data sets of three campaigns (Convective and Orographically-induced Precipitation Study (COPS)/ETReC, THORPEX (The Observing System Research and Predictability Experiment) Pacific Asian Regional Campaign (T-PARC), and International Polar Year (IPY)-THORPEX), generated by the WALES DIAL which was installed nadir-viewing on board the DLR Falcon research aircraft. The data sets start 600 m below the aircraft where full overlap between the laser beam and the telescope field of view is given. Spectral impurity of the laser [Wirth *et al.*, 2009] is corrected taking advantage of all three online wavelength return signals. Profiles with ambiguous results between the different online signals or with unstable laser operation, which is monitored and recorded together with the data, were discarded at this stage. Before calculating the humidity profiles from the DIAL equation, uncorrelated instrumental noise was reduced by averaging the returned online and offline signals. In this study, measurements are horizontally averaged to 2–7 km. Based on the fact that the DIAL cannot perform measurements under optically thick clouds, small data gaps were filled by linear interpolation. The resulting data set comprises 20 flights with lengths ranging from 225 to 1300 km. The DIAL equation is applied with an effective vertical resolution of 150 m, and the vertical range of water vapor profiles starts from 1.5 km up to a maximum of 10.4 km height. Considering all levels of all flights, we analyzed 522 water vapor time series with a total length of about 370,000 km throughout the troposphere (see also Table 1). The measurements of specific humidity are of high accuracy, with errors expected to be less than 5–7% [Bhawar *et al.*, 2010]. In principle, the signal quality decreases with increasing distance from the aircraft. By using the lagged

autocorrelation method [Kiemle *et al.*, 1997; Lenschow *et al.*, 2000] by which fictitious from natural variance can be separated, we have found that in the analyzed vertical range between 1.5 and 10.4 km, this decrease is nearly fully compensated by increasing water vapor and aerosol densities, as observed in earlier studies [cf. Kiemle *et al.*, 2011]. On average, over all 20 flights, the statistical uncertainty caused by uncorrelated instrumental noise lies around 5% and shows only a weak height dependency.

### 2.1. COPS/ETReC (2007)

[12] The aim of the Convective and Orographically-induced Precipitation Study (COPS), which took place in summer 2007 in middle and southwest Europe, was to improve the skill to forecast convective precipitation over complex mountainous terrain in the summer season [Wulfmeyer *et al.*, 2011]. Therefore, the influence of small-scale inhomogeneities of humidity, temperature, and wind on convection initiation was observed and investigated. For this study, we use the water vapor measurements performed during flights of the DLR Falcon equipped with nadir-pointing water vapor lidar [Kiemle *et al.*, 2011]. The seven flights analyzed in this study took place in the period 8 July to 1 August 2007 (see also Figure 1a). The typical weather situations during the campaign included cases with surface-forced convection in high pressure and synoptically forced convection in warm advected air masses ahead of an upper-level trough.

### 2.2. IPY-THORPEX (2008)

[13] The 3 week Norwegian IPY-THORPEX campaign which was part of the International Polar Year (IPY) took place between 25 February and 17 March in 2008 with the DLR Falcon as the main measurement platform of the field campaign [Wagner *et al.*, 2011]. Most flights took place over Scandinavia and near Spitzbergen (see Figure 1b). The aim was to yield detailed observations of polar lows, Arctic fronts, and orographic low-level jets near Spitzbergen, the coast of Northern Norway, and the east of Greenland [Kristjansson *et al.*, 2011]. In particular, the DIAL system on board the DLR Falcon served for investigations of Arctic humidity structures. The seven analyzed flight segments with 160 time series have a total length of 134,010 km and cover a vertical range from 1.5 to 9.3 km.

### 2.3. T-PARC (2008)

[14] During the THORPEX (The Observing System Research and Predictability Experiment) Pacific Asian Regional Campaign (T-PARC), which took place in the western North Pacific basin from August to October 2008, the WALES demonstrator collected a unique set of water

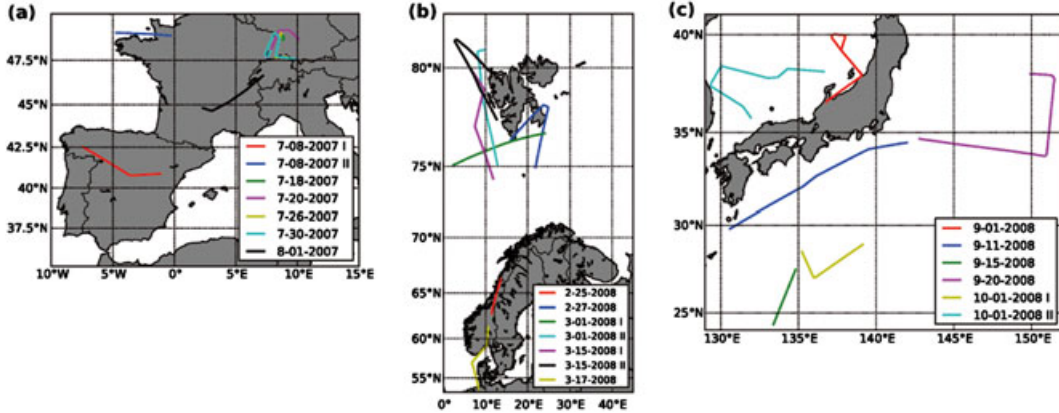


**Figure 1.** Falcon flight paths of the analyzed segments of (a) the COPS/ETReC campaign in 2007, (b) the IPY-THORPEX campaign in 2008, and (c) the T-PARC campaign in 2008.

vapor profiles [Harnisch *et al.*, 2011]. T-PARC focused on various aspects of typhoon activity, including formation, intensification, structure change, motion, and extratropical transition. The 25 research flights during the period 26 August to 1 October 2008 were undertaken. Six flights (Figure 1c) with largest horizontal and vertical observational coverage were selected for the present study, giving 267 time series with a total length of 173,480 km and a vertical range from 2 to 10 km.

### 3. The Structure Function Method

[15] As a basis for our analysis, we calculate the one-dimensional horizontal structure function [e.g., Davis *et al.*, 1994]

$$S_q(r) = \langle |f(x_i + r) - f(x_i)|^q \rangle \quad (1)$$

for different orders  $q$ .  $\langle \rangle$  denotes an ensemble mean over all pairs of points separated by a distance  $r$ . In detail, we started the calculation of structure function by using a distance  $r = 1$ , which is the flight distance covered by the DLR Falcon between two adjacent elements of the time series  $f(x_i)$  with  $N$  equidistant elements. In general, for a separation  $r$ , the absolute values of  $N - r$  pairs of points, the so-called increments, are calculated. In practice, because of the finite size of flight segments, the ensemble mean is approximated by the arithmetic mean:

$$S_q(r) = \frac{1}{N-r} \sum_{i=1}^{N-r} |f(x_i + r) - f(x_i)|^q. \quad (2)$$

This routine is repeated for increasing  $r$  from 1 up to  $N - 1$  and for higher orders  $q$ , ending with  $q = 5$ . Finally, we identify scaling behavior as a power law dependence of structure functions on length scale ( $S_q(r) \propto r^{\zeta_q}$ ). The structure function exponent  $\zeta_q$  is determined by linear least square fits to the log-log structure functions of all orders between 5 to 100 km. To check whether the power law fit is exact enough to indicate scaling, Pressel and Collins [2012] introduced an ad hoc lower bound on the coefficient of determination  $R^2$ . This method is also known as  $R$ -squared and can be interpreted as the goodness of fit of a linear regression. In this study, the lower bound on  $R^2$  of 0.95 is adopted for the analysis.

[16] As shown in Figure 1, many flight tracks contain aircraft direction changes which lead to nonuniform

sampling and therefore influence the structure function analysis (see equation (1)). We have found, by eliminating the changes of direction that the statistical uncertainty of the scaling exponents due to aircraft direction changes is at most about 5%.

[17] Figure 2 (middle) shows two examples of structure functions up to fifth-order, computed as described above. The red lines are the least square fit results, with slope  $\zeta_q$  and goodness of fit  $R^2$ . For estimating the uncertainties of the slope  $\zeta_q$ , we calculate the variance of the slope  $\zeta_q$  by using the chi-square merit function [Press *et al.*, 2007]. Since for increasing values of  $r$ , the number of increments  $|f(x_i + r) - f(x_i)|$  decreases, the weighting goes in favor of the smaller scales. On the other hand, Figure 2 (middle) shows that for increasing values of  $r$ , the density of sampling points increases in the log-log plot, giving more robustness to the linear fit and the scaling exponent in the larger scales. Also apparent is the increasing uncertainty of the scaling exponent and of the linear fit for increasing order  $q$ .

[18] In this study, we focus the discussion on the first-order scaling exponent  $\zeta_1$  for two reasons. First, the first-order structure function is more robust than higher-order structure functions with respect to outliers in the increment  $|f(x_i + r) - f(x_i)|$ . Second, the first-order structure function allows for scaling relations that are naturally connected to the Hurst exponent  $H$  in the theory of turbulence which aids the physical interpretation. In the following, we use  $H$  instead of  $\zeta_1$ .

[19] Less emphasis will be placed on the second-order structure function scaling exponent of water vapor which is equivalent to the slope of the power spectrum, although the values are included in Tables 2 and 3, to permit comparisons with previous studies. As noted by Marshak *et al.* [1997], different processes can have identical spectra. For example, white noise and randomly positioned delta functions exhibit both a flat Fourier spectrum, but their spatial structure is completely different, with very intermittent variability in the latter case.

[20] Scaling exponents of higher-order structure functions can be used to characterize intermittency. In Figure 2 (bottom), intermittency is described by the deviation of the parameterized dashed curve from the linear curve. By using an empirical two-parameter function introduced by Pierrehumbert [1996], we fit the dashed curve through the

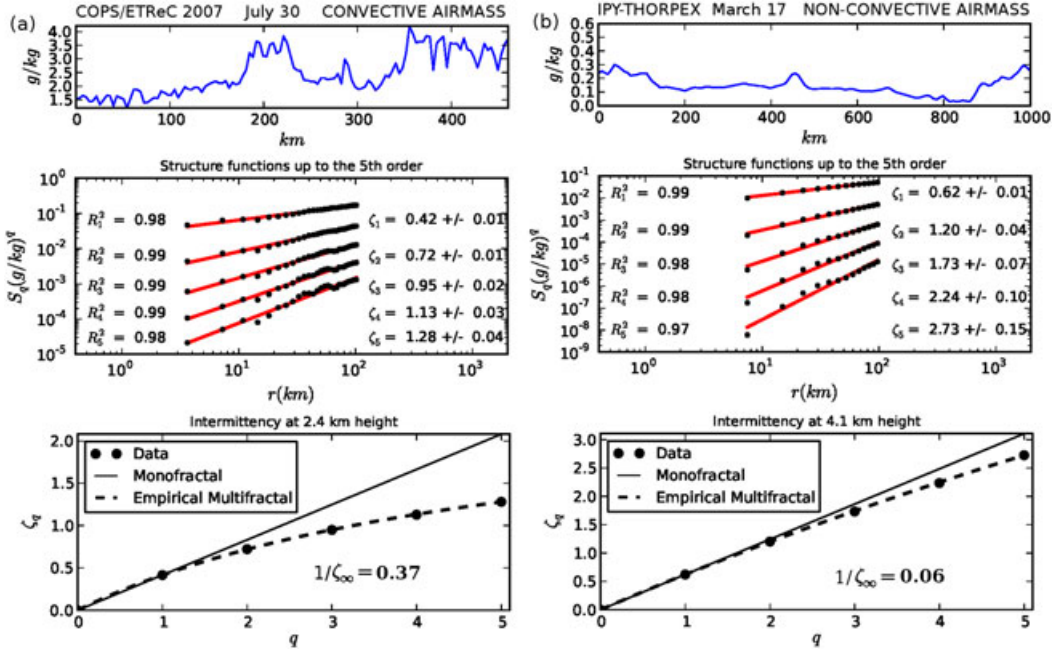


**Figure 2.** Structure function analysis of two example time series in the (a) convective and (b) nonconvective regime at (Figure 2a) 2.4 and (Figure 2b) 4.1 km height. (top) Representative specific humidity data samples, (middle) structure functions of the time series up to fifth-order, and (bottom) average slopes  $\zeta_q$  versus order  $q$ . The intermittency  $1/\zeta_\infty$  is calculated using a parameterization of *Pierrehumbert* [1996]; lower values indicate lower intermittency.

different order scaling exponent values, in order to obtain the intermittency parameter  $1/\zeta_\infty$ . This value provides a compact proxy for the evolution of the scaling exponents of structure functions of orders higher than 3. One can say that the more concave the curve is, the more intermittent the process [Calif and Schmitt, 2012]. If  $1/\zeta_\infty$  goes to zero, the dashed curve in Figure 2 (bottom) tends toward a linear slope, and intermittency becomes also zero, which is known as monoscaling or monofractal behavior. Increasing values of  $1/\zeta_\infty$  correspond to larger probabilities that the field contains jump discontinuities.

## 4. Results

### 4.1. Factors Influencing the Scaling Exponents

[21] The two-dimensional water vapor lidar cross sections of 20 flights collected in different regions of the world and during different seasons of the year contain a multitude of meteorological weather situations. The complex dynamics of water vapor in the troposphere are linked to the weather situations in terms of source and sink processes from convective clouds on the kilometer scale to cloud systems

associated with motions on scales of thousand or more kilometers, as well as advection of water vapor as a passive tracer outside of clouds [Emanuel and Pierrehumbert, 1996]. In Figure 3, a variety of tropospheric water vapor structures can be seen in the two-dimensional water vapor scans made by the DIAL on board the DLR Falcon. Figure 3a shows a very dry polar air mass with a shallow convective layer underneath a stable stratified troposphere. In contrast, the water vapor section in Figure 3b shows the influence of a tropical cyclone, with large and variable moisture content throughout the troposphere. Figure 3c was observed in midlatitude summer over land and shows large, vertically coherent moisture anomalies. A final example is shown in Figure 3d, where a filament of dry air extends from the upper troposphere to the boundary layer in a subtropical region. Such a large range of behaviors is not surprising given the various latitudes, seasons and orographic conditions of the field campaigns where the measurements were made. With this large data set, we will reexamine the conclusion of *Fischer et al.* [2012] that there is a clear distinction of the scaling exponents between air masses with and without convective clouds, and consider the possibility that other

**Table 2.** Characteristics and Statistical Properties (Arithmetic Mean With Standard Deviation) of the Time Series in Convective Air Masses<sup>a</sup>

Campaign	$L$ (km)	$N$	$\zeta_1$ ( $H$ )	$\zeta_2$	$1/\zeta_\infty$
COPS/ETReC	21,975	58	$0.32 \pm 0.12$	$0.61 \pm 0.22$	$0.34 \pm 0.19$ ( $N = 34$ )
T-PARC	22,630	34	$0.36 \pm 0.08$	$0.67 \pm 0.15$	$0.25 \pm 0.12$ ( $N = 19$ )
IPY-THORPEX	10,110	19	$0.43 \pm 0.08$	$0.74 \pm 0.16$	$0.23 \pm 0.09$ ( $N = 12$ )
Total/averages	54,715	111	$0.35 \pm 0.11$	$0.65 \pm 0.20$	$0.30 \pm 0.16$ ( $N = 65$ )

<sup>a</sup> $L$  is the total length of the time series,  $N$  is the number of time series.

**Table 3.** As Table 2 in Nonconvective Air Masses

Campaign	$L$ (km)	$N$	$\xi_1$ ( $H$ )	$\xi_2$	$1/\xi_\infty$
COPS/ETReC	22,585	39	$0.57 \pm 0.13$	$1.04 \pm 0.25$	$0.12 \pm 0.09$ ( $N = 33$ )
T-PARC	167,930	231	$0.63 \pm 0.10$	$1.20 \pm 0.19$	$0.09 \pm 0.07$ ( $N = 132$ )
IPY-THORPEX	123,902	141	$0.65 \pm 0.09$	$1.20 \pm 0.18$	$0.13 \pm 0.11$ ( $N = 87$ )
Total/averages	314,417	411	$0.63 \pm 0.10$	$1.19 \pm 0.19$	$0.11 \pm 0.09$ ( $N = 252$ )

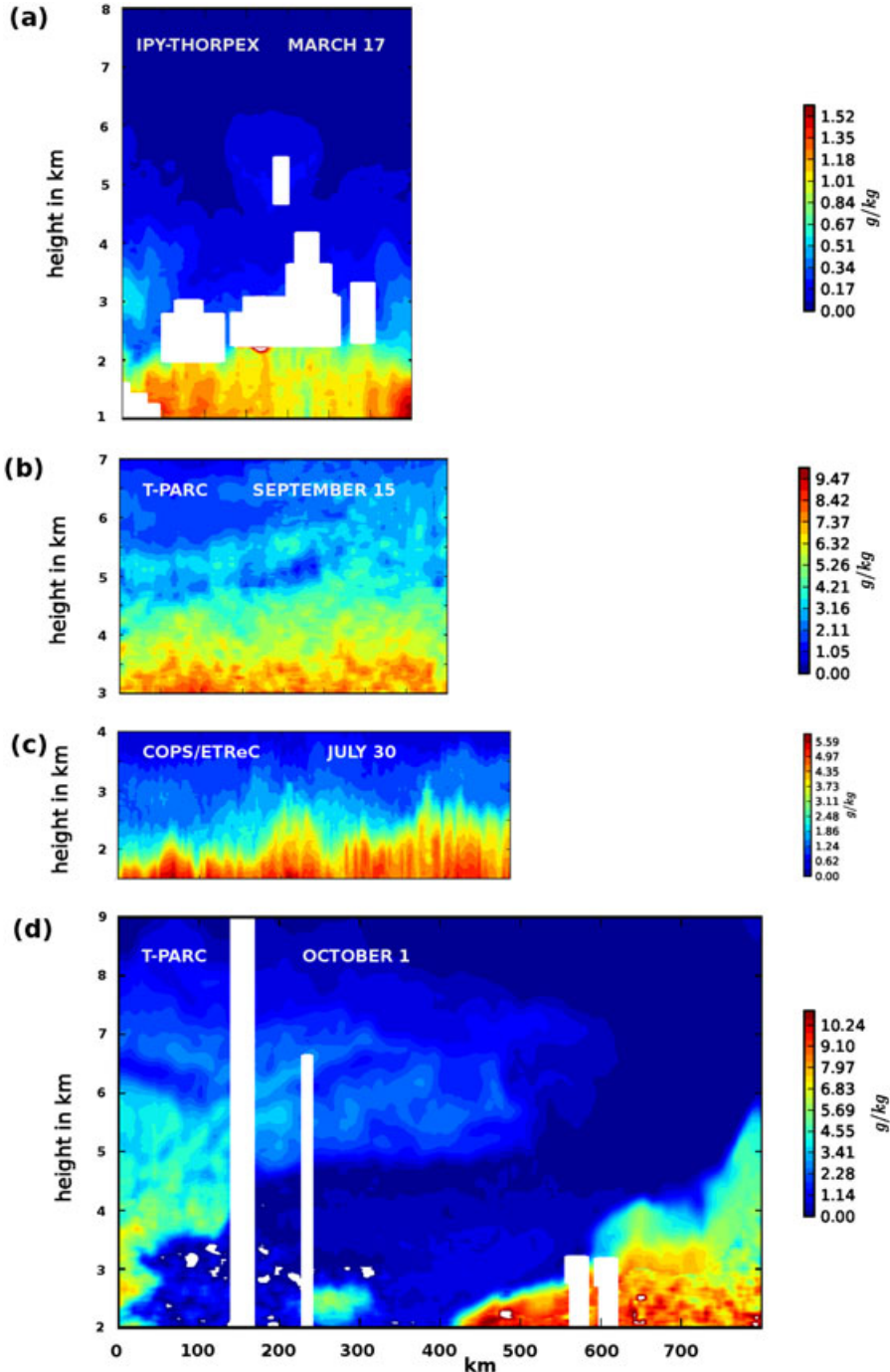


**Figure 3.** Lidar measurements of the water vapor field of four different flight segments from three campaigns.

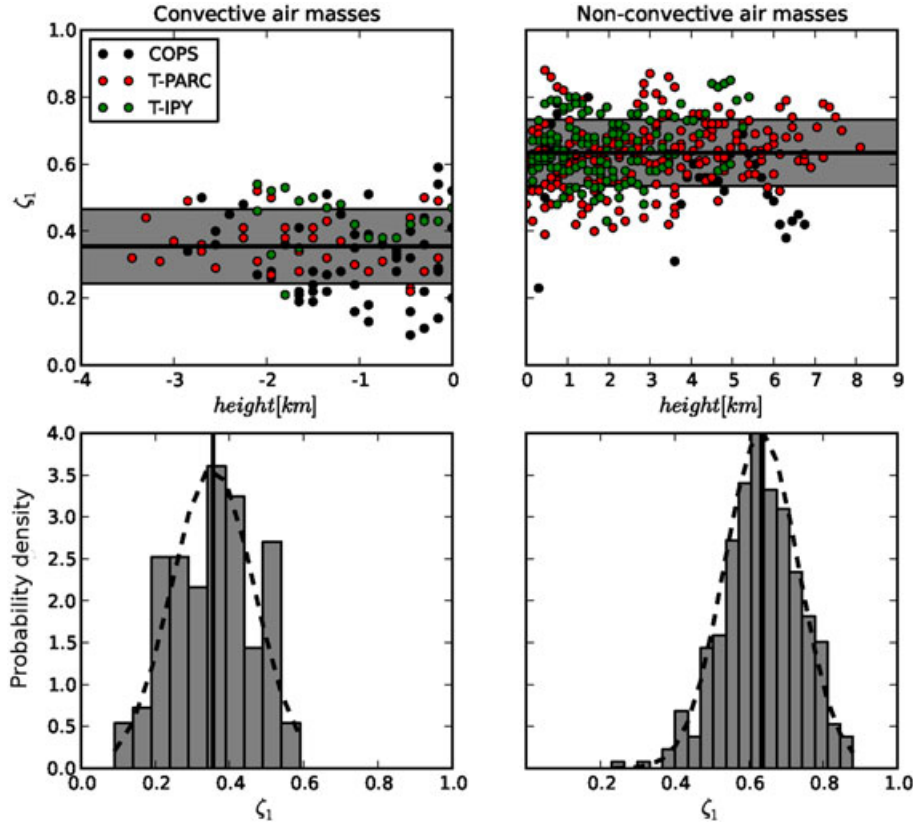


**Figure 4.** (top) First-order scaling exponents of (left) convective and (right) nonconvective time series of all three campaigns. The  $x$  axis is the height relative to cloud top height. Horizontal line is the mean value with the standard deviation (shaded area). (bottom) The associated histograms, which are normed to unity integral, for the two regimes. Vertical solid line is the mean value; dashed line is the fitted normal distribution.

differences between the campaigns could play an equal or more important role.

#### 4.2. Distribution of Scaling Exponents

[22] Air masses are classified into convective or non-convective categories using the lidar backscatter intensity [Fischer *et al.*, 2012]. In a first step, we identify the cloud top level by using the off-line reference wavelength. In a second step, we divide the observed water vapor time series into two categories. One category contains all time series below and the other all time series above the top of the highest cloud (note that some lidar cross sections contain only one category). Figure 2 (top) shows typical examples of time series from each of the two regimes. The qualitatively different appearance of the two series in the top panels is confirmed by smaller scaling exponents and larger intermittency for the convective air mass (left panels). Note that the number of time series in nonconvective air masses (411) is almost 4 times higher than in convective air masses (111) because the flight campaigns intentionally avoided cloudy regions and because the vertical range of convection is often much smaller than the vertical range of the nonconvective air masses.

[23] The distribution of values for the scaling exponent  $H$  of the first-order structure function over a range of scales from 5 to 100 km is shown in Figure 4 (top). The  $x$  axis is the height relative to cloud top level where negative values stand

for the convective layers and positive values for the layers above convection. In clear-sky case, the surface height was used as the cloud top height. Figure 4 (top left) represents all scaling exponents in convective air masses, while Figure 4 (top right) plots all scaling exponents in nonconvective air masses. The mean value in the convective regime,  $H = 0.35 \pm 0.11$ , is smaller than that of the nonconvective regime,  $H = 0.63 \pm 0.10$ , i.e., the mesoscale variability of water vapor on horizontal scales from 5 to 100 km is clearly different from the observed universal scaling law behavior on larger scales [e.g., Nastrom *et al.*, 1986]. We hypothesize that the water vapor fluctuations in convective air masses result from convective plumes and motions. Therefore, a smaller Hurst exponent as expression of a rougher water vapor field with higher small-scale variance can be expected. On the other hand, in free tropospheric layers without convection, water vapor can be regarded as an advected, conservative tracer which leads to a drop off of small-scale humidity variance and thus steepens the spectrum and structure function slopes. Also significant is the fact that the change in mean value occurs abruptly at the cloud top height. There is no evidence of a gradual transition in these high-resolution data. This supports our hypothesis that the different Hurst exponents are caused by different physical mechanisms.

[24] There is some overlap in the distributions between the two regimes, raising the question of whether the difference is statistically significant [Press *et al.*, 2007]. A

difference of means can be very small compared to the standard deviation, and yet very significant, if the number of data points is large. Conversely, a difference may be moderately large but not significant, if the data is sparse. We use the  $F$  test and the Student's  $t$  test to decide if the mean values of both distributions are significantly different. In our data set, the high  $P$  value (0.86) of the  $F$  test means that the two distributions have the same variances. The Student's  $t$  test gives us a very low  $P$  value ( $\ll 0.001$ ) which means that the difference of the means of the first-order structure function is highly significant.

[25] Testing the significance of the difference between the scaling exponents of the two regimes has been accomplished successfully up to the fifth-order function. For completeness, the mean value of the second-order scaling exponent which is the equivalent of the slope of the power spectrum is presented for the two regimes. The mean exponent value in the convective regime is found to be close to two thirds. In contrast, the mean value in the nonconvective air masses is approximately twice that value (1.19) (see also Tables 2 and 3).

[26] The distribution of the observed intermittency is also found to be significantly different between the two regimes: high intermittency prevails in convective air masses ( $\zeta_\infty = 0.30$ ) and low intermittency in nonconvective air masses ( $\zeta_\infty = 0.11$ ). These results give evidence that in convective air mass, injection of humidity plumes leads to a highly intermittent water vapor field, in contrast to the more monoscaling behavior found in nonconvective air mass where cascading to smaller scales does homogenize the water vapor field on scales up to 100 km.

### 4.3. Structure Functions in Convective Air Mass

[27] The histogram of the first-order scaling exponents  $H$  of the convective air masses (see Figure 4, bottom left) has a maximum near the mean value of  $H = 0.35 \pm 0.11$ . Splitting up the scaling exponent into the three campaigns shows that the values observed for IPY-THORPEX ( $H = 0.43 \pm 0.08$ ), T-PARC ( $H = 0.36 \pm 0.08$ ), and COPS/ETReC ( $H = 0.32 \pm 0.12$ ) are very similar (see Table 2). There is only a very small tendency (approximately as large as the standard deviation) for larger scaling exponents during winter in polar regions (IPY-THORPEX) in contrast to T-PARC and COPS/ETReC in summer, but it is not clear if this has a seasonal, latitudinal, or even topographical (difference between land and ocean) origin (see also Figure 4, top left). *Pressel and Collins* [2012] showed in a global analysis of AIRS data that there is little seasonal variability in the scaling exponents. The results of the present study suggest that latitudinal, seasonal, and topographical influences on the scaling exponents are small in comparison to the impact of the different dynamical processes in convective and nonconvective air masses. Such influences could exist, but the present data set does not allow their verification. Apparently, the physical mechanism of convection in different environments produces very similar power laws with a Hurst exponent  $H$  of about one third. Interestingly, the low value of the scaling exponent  $H$  found for the convective regime  $R_{\text{conv}}$  is similar to values observed for mesoscale variability in the convective boundary layer [*Cho et al.*, 2000; *Kahn et al.*, 2011; *Pressel and Collins*, 2012]. It is unlikely that our data set contains any significant contribution from

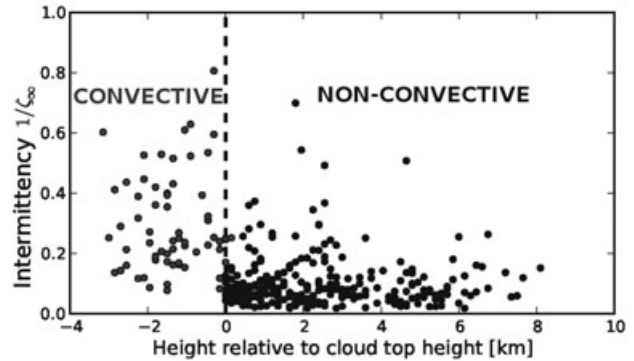


**Figure 5.** The intermittency of convective and nonconvective time series of all three campaigns. The  $x$  axis is the height relative to cloud top height.

the boundary layer, since the lowest 2–3 km of the troposphere are generally excluded due to low data quality and the top of the boundary layer is usually characterized by shallow convective cumulus. It appears that the dynamics of convective clouds in the free troposphere generate water vapor structures similar to the boundary layer, resulting in a similar scaling exponent.

[28] The structure function method has the potential to describe the intermittency of water vapor distributions, as  $1/\zeta_\infty$  quantifies the intermittency, whereby the full hierarchy of exponents  $\zeta_q$  is necessary to qualify it [*Davis et al.*, 1994]. In principle, intermittency has been used as a description of the tendency of passive tracers to concentrate in localized structures separated by jump discontinuities [*Shraiman and Siggia*, 2000; *Tuck et al.*, 2003]. Similarly, *Calif and Schmitt* [2012] define intermittency as a property exhibiting large fluctuations at all scales, with correlated structure. Such properties would be expected as a result of injection of moisture by coherent vertical plumes in a region of convection. On the other hand, if intermittency is low, the water vapor field has monoscaling behavior which is expected for a passive tracer advected by a spatially smooth flow [*Chertkov et al.*, 1995; *Pierrehumbert*, 1994].

[29] By using the parameterization of *Pierrehumbert* [1996], intermittency  $1/\zeta_\infty$  could be calculated for 65 time series of the convective regime. Note that this is only about 60% of the available time series because the remaining 40% did not achieve the lower bound on  $R^2$  of 0.95 which was defined to identify power law scaling. The mean value of intermittency in the convective regime, which is nearly identical in all three campaigns, is  $0.30 \pm 0.16$  (see Table 2). In Figure 5, some outliers in the convective regime with values lower than 0.1, i.e., low intermittency, become apparent, although the majority of the time series are described by high intermittency ( $1/\zeta_\infty > 0.2$ ). Note that despite the appearance of larger scatter in Figure 5 for the convective cases, the relative standard deviation is only 10% larger than for the nonconvective cases. In summary, these results show that the water vapor field in convectively influenced air mass in three very different geographical regions behaves similarly with respect to intermittency on horizontal scales up to 100 km.

### 4.4. Structure Functions in Nonconvective Air Mass

[30] The distribution of first-order scaling exponents for the time series of nonconvective air masses, shown in

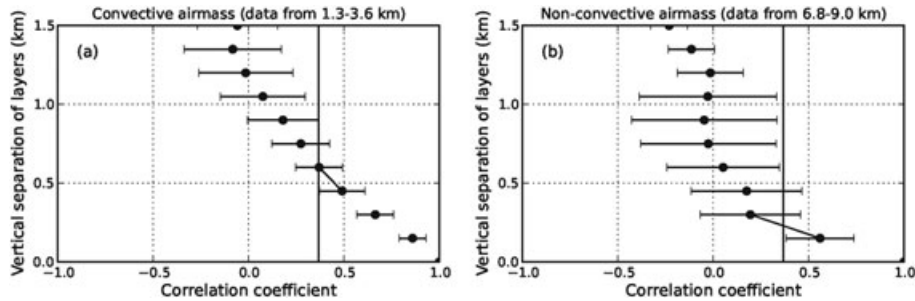


**Figure 6.** Dots depict the mean correlation coefficient of water vapor versus vertical separation. (a) Results for a 250 km segment on 30 July in 2007 between 1.3 and 3.6 km (convective case). (b) Results for a 250 km segment on 17 March in 2008 between 6.8 and 9.0 km (nonconvective case). The error bars indicate the standard deviation of the raw data. The vertical solid line shows the  $e^{-1}$  threshold value. The correlation length is calculated by the linear fit between two points above and below the threshold value.

Figure 4 (bottom right), are unimodal with a peak occurring very near to 0.6. Averaged over the whole data set of the nonconvective regime, we find a mean value of  $H = 0.63 \pm 0.10$ . As in the convective regime, the observations of the three campaigns agree within their uncertainty ranges (see Table 3). These results confirm that there is remarkably little regional variation in the observed exponents. Furthermore, the Hurst exponents found in this study are consistent with the results of *Pressel and Collins* [2012], who report values around 0.55 in the free troposphere (500 hPa level) over horizontal scales from 50 to 500 km. Our findings are consistent with the hypothesis that the absence of small-scale convective sources in the nonconvective regime lead to fewer small-scale water vapor fluctuations, generating smoother time series and therefore higher scaling exponents.

[31] The intermittency is very small in the nonconvective regime ( $1/\zeta_\infty = 0.11 \pm 0.09$ ) (see also Figure 5). A fraction of 40% of the calculated fifth-order structure functions does not exhibit power law dependence according to the criterion of  $R^2 \geq 0.95$ . Approximately 75% of the intermittency values are smaller than 0.2. Nevertheless, there are some outliers with values larger than 0.3 (see Figure 5), but a physical explanation is still not evident. At least, we can exclude that these measurements are from inside the boundary layer. In principle, the observed intermittency values are mostly lower (less intermittent time series) than the values found by *Cho et al.* [2000] for the extratropical free troposphere ( $1/\zeta_\infty = 0.21$ ). It should be noted, however, that *Cho et al.* [2000] investigated only 11 free tropospheric extratropical time series, which may have partly been influenced by convection.

## 5. Vertical Correlation Length of Water Vapor Structures

[32] Taking advantage of the high vertical resolution (200 m) and accuracy (5–7%) of the water vapor observations from DIAL, in this section, we focus on the vertical structure of humidity. In principle, we quantify the correlation between water vapor time series at varying heights, comparable to the method used by *Thurai et al.* [2011]. Therefore, we calculate the vertical correlation length of vertically adjacent levels, i.e., the depth over which the correlation coefficient of water vapor time series in separate levels falls to  $e^{-1}$  [*Hogan and Illingworth*, 2002]. Note that

the exponential decay of humidity in the vertical would tend to dominate the computed length scale even in the presence of convectively induced vertically coherent structures. We counter this problem by subtracting the mean humidity value from each horizontal time series before correlating. From simple physical reasoning, we hypothesize that water vapor features are correlated over longer vertical distances in the vicinity of convective clouds where vertical up and downdrafts dominate. In contrast, in regions without convective clouds, the water vapor field might have short vertical correlation lengths due to vertical shear in the large-scale advecting winds.

[33] The analysis of the vertical correlation length between time series at different heights of the three campaigns is carried out for the convective and nonconvective regimes. The average correlation length for the convective regime ( $L_{\text{conv}} = 0.39 \pm 0.14$  km) is longer than that of the nonconvective regime ( $L_{\text{nonconv}} = 0.31 \pm 0.12$  km), but with low significance. This may mean that vertical coherent water vapor structures caused by convection have only weak influence on the vertical correlation length in the water vapor field. On the other hand, the technical restriction that the DIAL water vapor observations are missing directly below optically thick clouds may mean that the observed water vapor field does not fully describe the existing vertical coherences, despite the fact that convective turbulence with upward and downward motions of water vapor is also active in the atmosphere around convective clouds [*Kottmeier et al.*, 2008], where the water vapor field is observed by the DIAL. It is also possible that the reduction of vertical coherence by advection in a flow with vertical shear, which is also active in convective regions, may act rapidly enough to reduce the correlation length to values similar to those found in nonconvective air masses [see also *Cho et al.*, 2003]. The results might be clearer if we had data in and beneath the clouds, where correlation should be strongest. For that reason, a future campaign with additional flight-level aircraft data could widen the frame of the results of this study.

[34] While the difference in vertical correlation length between convective and nonconvective air masses is small when averaged over the entire data set, it can be more apparent when comparing individual case studies, such as the examples shown in Figures 2 and 6. On 30 July in 2007 (see Figure 3c), the DLR Falcon measured water vapor over southwest Germany. The weather during the flight is

characterized by shallow cumulus up to a height of 3.5 km. Figure 3c shows the two-dimensional water vapor field after interpolating the gaps caused by clouds and horizontal averaging to about 5 km resolution. Figure 6a shows the mean correlation coefficient between water vapor time series at varying heights. On 17 March in 2008 (see Figure 3a), the DLR Falcon collected data between South-Norway and North-Germany. Above shallow cumulus, very dry air is advected. As seen in Figure 6b, the correlation decreases rapidly with height in this nonconvective air mass. To facilitate comparison, we consider data over a vertical range of 2.25 km in both cases. The correlation lengths  $L_{\text{conv}}$  and  $L_{\text{nonconv}}$  estimated from these figures are 0.60 and 0.23 km, showing a much longer vertical correlation length for the convective case.

## 6. Discussion and Conclusion

[35] In this study, structure functions throughout the troposphere (from 1.5 up to 10.4 km height) are computed from spatial increments of the instantaneous water vapor field observed by airborne DIAL. Water vapor structures of wintertime polar, summertime midlatitude, and subtropical regions are analyzed. The high horizontal (2–7 km) and vertical resolution (0.2 km) is sufficient to show horizontal structure function scaling from about 5–100 km. By using scaling exponents up to the fifth-order, intermittency is also calculated. Finally, the airborne DIAL water vapor observations are highly enough vertically resolved to calculate vertical correlation lengths in the tropospheric water vapor field.

[36] The analyzed observations in the paper of *Fischer et al.* [2012] show that first-order scaling exponents and the intermittency exhibit significant vertical variability during summertime over Europe. The present work gives an analysis of a much larger data set with a larger geographical extent, including data from a polar region and from a subtropical region. The conclusion of the earlier study that there exist two distinct scaling regimes, one in air masses where convection is present, and another where only large-scale advective processes occur, is confirmed. The analysis of the larger data set which includes substantially more weather situations at different geographical regions strengthens significantly the conclusions of the previous paper.

[37] The presence of convection at given height is determined through examination of the cloud tops seen by the lidar. The average first-order scaling exponent in convective air masses is lower than that of the nonconvective regime ( $R_{\text{conv}}: H = 0.35 \pm 0.11$  and  $R_{\text{nonconv}}: H = 0.63 \pm 0.10$ ). Conversely, the intermittency in convective air masses is higher ( $R_{\text{conv}}: 1/\zeta_{\infty} = 0.30 \pm 0.16$  and  $R_{\text{nonconv}}: 1/\zeta_{\infty} = 0.11 \pm 0.09$ ). Within the data set considered here, the scaling behaviors within the two regimes appear to be independent of latitude and height. In general, scaling exponents  $< 0.5$  have a rougher, more space filling appearance, while scaling exponents  $> 0.5$  are smoother and longer range correlated (see Figure 2).  $H \approx \frac{1}{3}$  seems to be a relatively universal characterization not only for the atmospheric boundary layer [*Cho et al.*, 2000] but also for layers above where the water vapor field is locally influenced by convective clouds.

[38] The physical picture that emerges is that small-scale motions in the boundary layer or in cumulus convection

above introduce localized, small-scale structures into the atmosphere, leading to a rougher, more intermittent moisture field. In contrast to the convective regime, where local variations establish the spatial variability of water vapor, the nonconvective regime is dominated by the large-scale flow. These passively advected layers exhibit first-order scaling exponents around 0.6. The intermittency is very low, i.e., there is a tendency of water vapor to exhibit monoscaling in nonconvective air masses as expected for a passive tracer advected by a spatially smooth flow [*Chertkov et al.*, 1995; *Pierrehumbert*, 1994].

[39] The scaling exponents determined here are not enough to clearly establish the underlying physical process. In contrast to turbulent cascade processes of kinetic energy where several theories exist, a quantitative theory that predicts the scaling exponents in a convectively influenced air mass is lacking. It is even possible that different physical mechanisms may result in a similar scaling exponent. On the other hand, the different scaling parameters identified here are strong evidence that the two regimes are dominated by different physical processes on spatial scales from 5 to 100 km.

[40] The results show that our physically based classification of the data set into convective versus nonconvective air masses leads to two scaling exponent regimes. We hypothesize that more small-scale variability due to convection, primarily localized, vertical convective moisture injection, leads to smaller scaling exponents and higher intermittency values than in nonconvective air masses. An alternative approach would be to apply thresholds to the scaling exponent values to separate the data into two classes. The scatter plots (Figures 4 and 5) show that the difference of the first-order scaling exponents between the two regimes is clear enough to make such an approach feasible. However, the determination of thresholds is subjective, and the intermittency value is quite scattered, since it is the result of two fitting procedures. We therefore did not select this approach.

[41] As a final test of the physical picture gained by the structure function analysis, we have computed vertical correlation lengths, in the expectation that the local convective circulations will produce structures that are more vertically coherent. A comparison of two case studies showed a longer correlation length for a convective situation than for a nonconvective one. Averaged over the entire data set, a longer mean correlation length was again found for the convective regime; however, the difference was not statistically significant. A larger data set will be required to definitively test the hypothesis.

[42] In the future, it would be helpful to collect more water vapor data in convective regimes, especially in and beneath clouds. While it is impossible for the DIAL system to measure through optically thick clouds, aircraft in situ measurement could also provide water vapor series in and beneath clouds. We would advocate a flight campaign where aircraft in situ measurements would be combined with airborne DIAL measurements. In an ideal case, the airborne DIAL would measure the water vapor field from the tropopause down to and in between convective clouds, while another aircraft would fly directly through the convective clouds measuring water vapor in the clouds and beneath. Since deep convection poses extended risks for aviation, the weather situation should be characterized by scattered,

developing moist convection. Such a campaign configuration could help to gain further insights on how the water vapor distribution in the free troposphere is affected by small-scale convective processes.

[43] Height-resolved structure functions of the tropospheric water vapor field could serve as an important diagnostic of numerical model performance. *Waite and Snyder* [2012] have shown a strong influence of moist processes on the mesoscale dynamical structures in simulations of an idealized baroclinic wave. The ability of a high-resolution numerical weather prediction model to reproduce the observed universal scaling behavior of the water vapor distribution will provide a strong test of the representation of dynamical and moist processes, independent of initial conditions.

[44] **Acknowledgments.** This work is part of the second part of the research grant SPP-1294 “High Altitude and Long Range Research Aircraft” (HALO) funded by the Deutsche Forschungsgemeinschaft (DFG). The data set used in this work arises from the DLR Falcon participation in COPS/ETReC which was supported by the Deutsche Forschungsgemeinschaft (DFG) in the frame of the SPP-1167 “Quantitative Precipitation Forecast.” During T-PARC, the DLR Falcon aircraft was sponsored by an international consortium from Germany, the United States, Japan, Korea, and Canada.

## References

- Bhavar, R., et al. (2010), The water vapour intercomparison effort in the framework of the convective and orographically-induced precipitation study: Airborne-to-ground-based and airborne-to-airborne lidar systems, *Q. J. R. Meteorol. Soc.*, *137*, 325–348.
- Bösenberg, J. (1998), Ground-based differential absorption lidar for water-vapor and temperature profiling: Methodology, *Appl. Opt.*, *37*, 3845–3860.
- Calif, R. (2011), *Stochastic Simulation for the Atmospheric Wind Using a Continuous Cascades*, vol. 8, pp. 24–28, IACSIT Press, Bali Island, Indonesia.
- Calif, R., and F. G. Schmitt (2012), Modeling of atmospheric wind speed sequence using a lognormal continuous stochastic equation, *J. Wind Eng. Ind. Aerodyn.*, *109*, 1–8.
- Chertkov, M., G. Falkovich, I. Kolokolov, and I. Lebedev (1995), Statistics of a passive scalar advected by a large-scale two-dimensional velocity field: Analytic solution, *Phys. Rev. E*, *51*, 5609–5627.
- Cho, J. Y. N., Y. Zhu, R. E. Newell, B. E. Anderson, J. D. Barrick, G. L. Gregory, G. W. Sachse, M. A. Carroll, and G. M. Albercook (1999), Horizontal wavenumber spectra of winds, temperature, and trace gases during the pacific exploratory missions: 1. Climatology, *J. Geophys. Res.*, *104*, 5697–5716.
- Cho, J. Y. N., R. E. Newell, and G. W. Sachse (2000), Anomalous scaling of mesoscale tropospheric humidity fluctuations, *Geophys. Res. Lett.*, *27*, 377–380.
- Cho, J. Y. N., R. E. Newell, B. E. Anderson, J. D. W. Barrick, and K. L. Thornhill (2003), Characterizations of tropospheric turbulence and stability layers from aircraft observations, *J. Geophys. Res.*, *108*(D20), 8784, doi:10.1029/2002JD002820.
- Corrsin, S. (1951), On the spectrum of isotropic temperature fluctuations in an isotropic turbulence, *J. Appl. Phys.*, *22*, 469–473.
- Cusack, S., J. M. Edwards, and R. Kershaw (1999), Estimating the subgrid variance, and its parameterization for use in a GCM cloud scheme, *Q. J. R. Meteorol. Soc.*, *125*, 3057–3076.
- Davis, A., A. Marshak, W. Wiscombe, and R. Cahalan (1994), Multifractional characterizations of nonstationarity and intermittency in geophysical fields: Observed, retrieved, or simulated, *J. Geophys. Res.*, *99*, 8055–8072.
- Emanuel, K. A., and R. T. Pierrehumbert (1996), Microphysical and dynamical control of tropospheric water vapor, in *Cloud Chemistry and Climate, NATO ASI Ser., Ser. I*, vol. 135, edited by P. J. Crutzen and V. Ramanathan, pp. 17–28, Springer, Berlin.
- Fischer, L., C. Kiemle, and G. C. Craig (2012), Height-resolved variability of midlatitude tropospheric water vapor measured by airborne lidar, *Geophys. Res. Lett.*, *39*, L06803, doi:10.1029/2011GL050621.
- Harnisch, F., M. Weissmann, C. Cardinali, and M. Wirth (2011), Experimental assimilation of DIAL water vapour observations in the ECMWF global model, *Q. J. R. Meteorol. Soc.*, *137*, 1532–1546, doi:10.1002/gj.851.
- Harris, D., E. Foufoula-Georgiou, K. K. Droegemeier, and J. Levit (2001), Multiscale statistical properties of a high-resolution precipitation forecast, *J. Hydromet.*, *2*, 406–418.
- Hogan, R. J., and A. J. Illingworth (2002), Parameterizing ice cloud inhomogeneity and the overlap of inhomogeneities using cloud radar data, *J. Atmos. Sci.*, *60*, 756–767.
- Kahn, B. H., and J. Teixeira (2009), A global climatology of temperature and water vapor variance scaling from the Atmospheric Infrared Sounder, *J. Climate*, *22*, 5558–5576.
- Kahn, B. H., et al. (2011), Temperature and water vapor variance scaling in global models: Comparisons to satellite and aircraft data, *J. Atmos. Sci.*, *68*, 2156–2168.
- Kiemle, C., G. Ehret, A. Giez, K. J. Davis, D. H. Lenschow, and S. P. Oncley (1997), Estimation of boundary layer humidity fluxes and statistics from airborne differential absorption lidar (DIAL), *J. Geophys. Res.*, *102*, 29,189–29,203.
- Kiemle, C., M. Wirth, A. Fix, S. Rahm, U. Corsmeier, and P. Di Girolamo (2011), Latent heat flux measurements over complex terrain by airborne water vapour and wind lidars, *Q. J. R. Meteorol. Soc.*, *137*, 190–203.
- Kottmeier, C., et al. (2008), Mechanisms initiating deep convection over complex terrain during COPS. Special issue on quantitative precipitation forecasting, *Meteorol. Z.*, *17*, 931–948.
- Kristjánsson, J. E., et al. (2011), The Norwegian IPY-THORPEX: Polar lows and arctic fronts during the 2008 Andoya campaign, *Bull. Amer. Meteor. Soc.*, *92*, 1443–1466, doi:10.1175/2011BAMS2901.1.
- Lenschow, D. H., V. Wulfmeyer, and C. Senff (2000), Measuring second-through fourth-order moments in noisy data, *J. Atmos. Ocean. Technol.*, *17*, 1330–1347.
- Lovejoy, S., A. Tuck, and D. Schertzer (2010), Horizontal cascade structure of atmospheric fields determined from aircraft data, *J. Geophys. Res.*, *115*, D13105, doi:10.1029/2009JD013353.
- Marshak, A., A. Davis, W. Wiscombe, and R. Cahalan (1997), Scale invariance in liquid water distributions in marine stratocumulus. Part II: Multifractional properties and intermittency issues, *J. Atmos. Sci.*, *54*, 1423–1444.
- Monin, A. S., and A. M. Yaglom (1975), *Statistical Fluid Mechanics*, vol. 2, 683 pp., MIT Press, Cambridge.
- Nastrom, G. D., W. H. Jasperson, and K. S. Gage (1986), Horizontal spectra of atmospheric tracers measured during the global atmospheric sampling program, *J. Geophys. Res.*, *91*, 13,201–13,209.
- Pierrehumbert, R. T. (1994), On tracer microstructure in the large-eddy dominated regime, *Chaos Solitons Fract.*, *4*, 1091–1110.
- Pierrehumbert, R. T. (1996), Anomalous scaling of high cloud variability in the tropical Pacific, *G. Phys. Res. Lett.*, *23*, 1095–1098.
- Press, W. H., S. A. Teukolsky, W. T. Vetterling, and B. P. Flannery (2007), *Numerical Recipes: The Art of Scientific Computing*, 3<sup>rd</sup> ed., 1235 pp., Cambridge University Press, New York.
- Pressel, K. G., and W. D. Collins (2012), First-order structure function analysis of statistical scale invariance in the AIRS-observed water vapor field, *J. Climate*, *25*, 5538–5555.
- Schotland, R. M. (1974), Errors in the lidar measurement of atmospheric gases by differential absorption, *J. Appl. Meteorol.*, *13*, 315–331.
- Sherwood, S. C., R. Roca, T. M. Weckwerth, and N. G. Andronova (2010), Tropospheric water vapor convection and climate, *Rev. Geophys.*, *48*, doi:10.1029/2009RG000301.
- Shraiman, B. I., and E. D. Siggia (2000), Scalar turbulence, *Nature*, *405*, 639–646.
- Thurai, M., V. N. Bringi, Y. H. Lee, L. S. Kumar, J. D. Eastment, and D. Ladd (2011), Height-correlation analysis of data from an S-band zenith-pointing radar in Singapore. <https://ams.confex.com/ams/35Radar/webprogram/Paper191243.html>.
- Tjemkes, S., and M. Visser (1994), Horizontal variability of temperature, specific humidity, and cloud liquid water as derived from spaceborne observations, *J. Geophys. Res.*, *99*, 23,089–23,105.
- Tompkins, A. M., and J. Berner (2008), A stochastic convective approach to account for model uncertainty due to unresolved humidity variability, *J. Geophys. Res.*, *113*, D18101, doi:10.1029/2007JD009284.
- Tuck, A. F., S. J. Hovde, E. C. Richard, D. W. Fahey, R. S. Gao, and T. P. Boy (2003), A scaling of ER-2 data in the inner Arctic vortex during January–March 2000, *J. Geophys. Res.*, *108*, doi:10.1029/2001JD000879.
- Wagner, J. S., A. Gohm, A. Dörnbrack, and A. Schäfer (2011), The mesoscale structure of a polar low: Airborne lidar measurements and simulations, *Q. J. R. Meteorol. Soc.*, *137*, 1516–1531, doi:10.1002/gj.857.
- Waite, M. L., and C. Snyder (2012), Mesoscale energy spectra of moist baroclinic waves, *J. Atmos. Sci.*, *70*, 1242–1256, doi:10.1175/JAS-D-11-0347.1.
- Wang, H., G. Feingold, R. Wood, and J. Kazil (2010), Modelling microphysical and meteorological controls on precipitation and cloud cellular

- structures in southeast Pacific stratocumulus, *Atmos. Chem. Phys.*, *10*, 6347–6362.
- Werner, C., and H. Herrmann (1981), Lidar measurements of the vertical absolute humidity distribution in the boundary layer, *J. Appl. Meteorol.*, *20*, 476–481.
- Wirth, M., A. Fix, P. Mahnke, H. Schwarzer, F. Schrandt, and G. Ehret (2009), The airborne multi-wavelength water vapor differential absorption lidar WALES: System design and performance, *Appl. Phys.*, *96*, 201–213.
- Wulfmeyer, V., et al. (2011), The Convective and Orographically-induced Precipitation Study (COPS): The scientific strategy, the field phase, and research highlights, *Q. J. R. Meteorol. Soc.*, *137*, 3–30, doi:10.1002/qj.752.
- Zhang, F., C. Snyder, and R. Rotunno (2003), Effects of moist convection on mesoscale predictability, *J. Atmos. Sci.*, *60*, 1173–1185.